Available online at www.sciencedirect.com
SCIENCE DIRECT®
Journal of Sound and Vibration 268 (2003) 85–101
JOURNAL OF SOUND AND VIBRATION
www.elsevier.com/locate/jsvi

Formulation and validation of a Ritz-based analytical model of high-frequency periodically layered isolators in compression

J.T. Szefi*, E.C. Smith, G.A. Lesieutre

Department of Aerospace Engineering, Rotorcraft Center of Excellence, The Pennsylvania State University, 229 Hammond Bldg., University Park, PA 16802, USA

Received 19 April 2002; accepted 5 November 2002

Abstract

Periodically layered isolators exhibit transmissibility "stop bands" or frequency ranges in which there is very low transmissibility. A two-dimensional axisymmetric model was developed to accurately predict the location of these stop bands for isolators in compression. A Ritz approximation method was used to model the axisymmetric elastic behavior of layered cylindrical isolators. A modal analysis was performed for a single elastomer and metal layer combination or cell. A modal synthesis approach was then used to obtain a model of an *n*-celled isolator, from which overall isolator modal properties are determined. This model of the dynamic behavior of layered isolators was validated with experiments. Analytical and experimental transmissibilities are compared for test specimens having identical elastomer components, but different geometries and different numbers of cells. In all cases, experimental and analytical transmissibilities are in close agreement at frequencies ranging from zero to those associated with the initial roll-off of the stop bands. For three and four cell cases, minimum stop band analytical transmissibilities lie below the minimum experimental measurements, although an experimental noise floor imposed a minimum transmissibility measurement of approximately 1.4×10^{-4}. Experiment suggests a practical isolator design could limit the minimum number of cells to three or four to ensure a pronounced stop band attenuation effect. In addition, analytical and experimental transmissibilities are compared for geometrically similar test specimens with differing elastomeric damping properties. The analytical and experimental results show that stop band effectiveness is not appreciably affected by the addition of modest damping.

1. Introduction

Dynamically tuned flexible mounts are frequently used for passive isolation of mechanical components subject to vibration. Elastomeric materials are incorporated into many mounts to

*Corresponding author.
E-mail addresses: szefi@psu.edu (J.T. Szefi), ecs@rcoe.psu.edu (E.C. Smith), g-lesieutre@psu.edu (G.A. Lesieutre).

0022-460X/03/$ - see front matter
doi:10.1016/S0022-460X(02)01574-2

provide a combination of low stiffness and moderate damping. Typical isolation mounts are designed to attenuate motion or force at low frequencies, usually below 100 Hz. The principles of vibration isolation in this frequency range are well understood. Elastomeric mounts employed for low-frequency isolation may be simultaneously subjected to higher-frequency, machine-generated vibro-acoustic energy. Standard isolation techniques, however, may not be appropriate for forcing frequencies much higher than the fundamental system frequency, due to the presence of wave effects. Wave effects occur at high frequencies when the elasticity and the distributed mass of the mount interact to create sharp transmissibility peaks [1].

Refs. [2,3] report that periodically layered metallic and elastomeric mounts are potential attenuators of dynamic stresses at high frequencies. The impedance difference between layers is the attenuation mechanism, in which an incident wave is scattered and essentially split into a reflected and refracted wave [4]. The device becomes increasingly effective with a larger impedance mismatch between the isolator materials.

A one-dimensional analysis of periodically layered isolators in compression is presented in Ref. [4]. Motivation for the research effort was isolation of reactor components and structures from seismic, impact, or other accident-induced loads. A time-domain solution was obtained for plane stress wave excitation through layered composites. The analysis makes use of continuity of stress and displacement at the layer interfaces. Plane longitudinal stress waves with particular wavelengths are attenuated in periodically layered elastic mounts, whereas no attenuation is exhibited by an undamped homogeneous elastic medium.

A one-dimensional analysis of layered isolators, based on the theory of shear waves in infinite, periodically layered media is presented in Refs. [2,3]. Floquet theory is used to solve the equations for the propagation of plane waves through a laminated system of parallel plates. The plates consist of two alternating materials, and the direction of propagation is normal to the plates. The theory predicts high-frequency ''stop bands'' within which vibratory energy is attenuated. The analysis includes a method for predicting the beginning and end frequencies of stop bands. Thus, the layered isolator behaves as a mechanical notch filter. The existence of the predicted stop bands was corroborated by testing of layered specimens in shear. The test specimens were of finite length, and therefore edge effects and reflections from the top and bottom layers were observed in the experiment. These effects, however, did not obscure the basic physical phenomenon of stop bands.

The effects of three-dimensional elasticity on periodically layered isolators in compression were examined in Ref. [5]. A detailed finite element analysis of periodically layered isolators was conducted to gain an improved understanding of three-dimensional effects on isolator performance. The isolator models consisted of alternating, cylindrical layers of elastomer and metal. Two-dimensional axisymmetric solid elements were used to model each layer of cylindrical isolators. Each element had eight nodes and 48 degrees of freedom. The first four mode shapes of a typical three-celled isolator are shown in Fig. 1.

The mode shapes of the isolator were then examined [5,6]. For an isolator with n cells, there are $(n-1)$ isolator modes below the beginning of the stop band. The stop band frequency range begins at the nth isolator mode and continues until the $(n+1)$th isolator mode. In the first n modes, each elastomer layer associated with these frequencies undergoes approximately uniform axial strain. In fact, the metal layers behave essentially like n discrete masses supported by n axial springs in series. Invariably, in the first mode, every elastomer layer exhibits either uniform

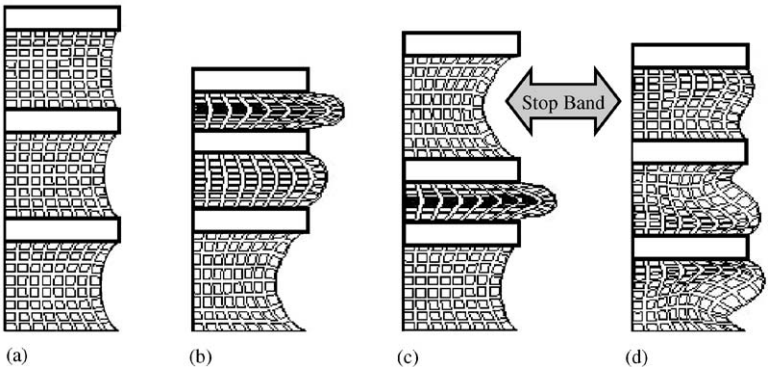

Fig. 1. First four axisymmetric mode shapes of a cylindrical three-celled isolator in compression. (a) mode 1, (b) mode 2, (c) mode 3, (d) mode 4.

tension or compression. In the next $(n-1)$ modes, the mode shapes of the individual layers are observed to contain different combinations of layerwise compression and tension. The $(n+1)$th mode (e.g., mode 4 in Fig. 1) is the first mode in which an elastomer layer exhibits a 'thickness' mode. Physically, this mode involves both tension and compression within the elastomer layer and minimal net axial motion of the constraining metal layers. This mode is associated with the end of the stop band frequency range.

The first three modes in Fig. 1 also exhibit significant lateral motion of the middle of each elastomer layer. This is due to fact that the upper and lower surfaces of each layer are constrained and that elastomeric materials are nearly incompressible. Consequently, the effective three-dimensional stiffness of each layer differs from that predicted by one-dimensional theory, which only addresses axial motion.

The utility of a 1-D "shape factor" for axisymmetric frequency predictions was investigated in Ref. [5]. The shape factor is a well-documented 1-D correction factor to account for the difference between the effective three-dimensional longitudinal stiffness and the stiffness predicted by one-dimensional theory. It is defined as the ratio of one bonded area to the force-free area of an elastomeric isolator. Essentially, the shape factor accounts for the discrepancy between the predicted quasi-static one-dimensional stiffness and the actual measured stiffness of an elastomer isolator. Ref. [5] found that the shape factor was not useful in predicting higher-frequency axisymmetric isolator modes. Errors of up to 100% were common for 1-D predictions of stop band frequencies.

A preliminary method was developed to predict stop band beginning and end frequencies in three dimensions [5]. A table look-up approach, which correlated 1-D frequencies to axisymmetric frequencies, was used. To accurately capture axisymmetric behavior, however, this approach required numerous axisymmetric FEM solutions for the entire design space of possible isolator geometries.

A design optimization methodology was also developed for layered isolators subject to quasi-static stiffness constraints [5,6]. A simulated annealing algorithm was employed to determine optimal material properties and layer thicknesses.

Experimental tests were also performed for various layered test specimens to verify the existence of stop bands in compression mounts [5,6]. Specimens were attached to a rigid base, which in turn

was attached to a mechanical shaker. An accelerometer was placed on top of the specimen, and another was placed on the base. The shaker inputs were a series of chirp signals over discrete frequency ranges. The accelerometer signals were then fed to a Fourier analyzer to determine transmissibility, and the stop band phenomenon was directly observed.

The overall goal of this research was to develop and experimentally validate a design methodology for periodically layered compression isolators. The primary objectives pursued to reach this goal were as follows:

(1) To develop a method for accurately predicting stop band beginning and end frequencies using an analytical, axisymmetric approach. The method should accurately capture the axisymmetric elastic behavior of vibrating cylinders and accommodate varying geometry, elastomer shape factor, and numbers of cells. In addition, the method should be able to calculate frequency-dependent transmissibility.
(2) To validate the analysis method by experiment. Experimental and analytical transmissibilities of layered test specimens having the identical elastomer, but different shape factors and different numbers of cells should be compared. The experimental and analytical transmissibilities of geometrically similar test specimens with differing elastomeric damping should also be compared.

2. Axisymmetric approximation method

In Ref. [5], a table look-up method was employed that required the construction of a database containing 1-D to 2-D axisymmetric frequency ratios. In the current work, a more general method is pursued for predicting the axisymmetric behavior of layered isolators. The method combines a Ritz approximation method with a component mode synthesis technique. For given isolator geometry, material properties, and number of cells, the axisymmetric stop band frequencies and the frequency-dependent transmissibility are calculated.

2.1. Natural frequencies of axisymmetric cylinders of finite length

A closed-form solution for natural modes of a vibrating cylinder is very difficult to obtain. Thus, several approximation methods have been pursued. In Ref. [7], Heyliger presents a technique for calculating the natural frequencies of the axisymmetric vibrations of isotropic and anisotropic cylinders of finite length. This method is general and can be applied to cylinders having a variety of boundary conditions and material properties.

The displacement components that describe the axisymmetric motion of an elastic cylinder can be expressed as

$$u = U_r(r, z), \quad w = U_z(r, z), \tag{1}$$

where u and w are independent displacements in the radial and axial directions, respectively. The strain components for axisymmetric motion can be written in cylindrical co-ordinates as

$$\varepsilon_1 = \varepsilon_{rr} = \frac{\partial u}{\partial r}, \quad \varepsilon_2 = \varepsilon_{\theta\theta} = \frac{u}{r}, \quad \varepsilon_3 = \varepsilon_{zz} = \frac{\partial w}{\partial z}, \quad \varepsilon_5 = \varepsilon_{rz} = \frac{\partial w}{\partial r} + \frac{\partial u}{\partial z} \tag{2}$$

The reader is referred to Ref. [7] for a detailed derivation of the equations of motion and possible boundary conditions. Analytical solutions to the equations of motion are difficult to obtain, and thus approximate solutions for the governing equations of motion are constructed by using the Ritz method, in which u and w are approximated by finite linear combinations of the form

$$u(r,z)=\sum_{k=1}^{N} b_k\phi_k^u(r,\,z), \quad w(r,\,z)=\sum_{k=1}^{M} d_k\phi_k^w(r,\,z). \tag{3}$$

Here ϕ_k^u and ϕ_k^w are known functions of position, n represents the number of terms for the displacement components, and b_k and d_k are constants.

Selection of the approximating functions, ϕ, is somewhat arbitrary [7]. Several requirements must be met, however, to guarantee that the approximations will converge to the mathematical solution. The functions ϕ_k^u and ϕ_k^w must meet the requirement of continuity as required by the variational statement, they must satisfy the homogeneous form of the essential, geometric boundary conditions, and they must be linearly independent and complete [7]. Because the variational problem is posed in energy form, the natural boundary conditions need not be explicitly satisfied.

In the current work, a single elastomer/metal cell is first modelled in a fixed-free condition. Multiple cell analyses will subsequently be combined in a complete isolator analysis. For numerical calculations, it is convenient to non-dimensionalize the cylinder geometry by mapping the original cylinder to a cylinder with a radius and half-height of 1 using the transformations $R=r/L_r$, and $Z=z/L_z$. Here, L_r is the cylinder radius and L_z is the cylinder half-height (see Fig. 2). At the bottom of the elastomer layer, the non-dimensional height is $z=-1$. The displacement at $z=-1$ of the elastomer layer is fixed at $u=0$ and $w=0$, as in Fig. 2. The metal layer, attached to the top of the elastomer layer at the non-dimensional height of $z=+1$, is modelled as a plane mass and is rigid and infinitely thin. Therefore, at $z=1$, $u=0$ and w is free, and the rigid plate translates vertically while remaining horizontal. This boundary condition effectively restricts any rocking motion of the top plate. The metal layer is modelled as a plane mass because all the strain energy is assumed to be in the elastomer layer.

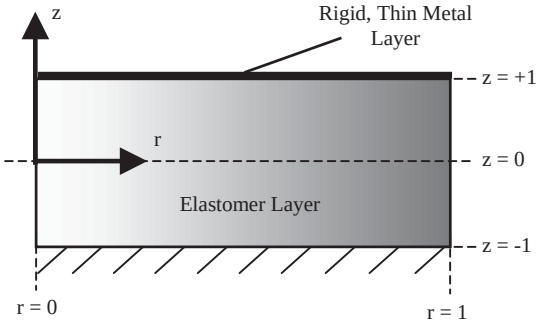

Fig. 2. Illustration of fixed-free boundary condition for a single cell.

Several different sets of functions could be selected to obtain an approximate solution. In this work, they must satisfy the boundary conditions $u = 0$, $w = 0$ at $z = -1$, and imposed conditions $u = 0$, w unconstrained and uniform at $z = 1$. A series of approximating functions were developed that consist of power series in the r and z directions and satisfy the preceding conditions. The functions for the u direction can be summarized as

$$\phi_k^u(r, z) = \sum_{i=1}^{n} \sum_{j=0}^{m} r^i(z+1)(z-1)z^j, \quad k = 1..[n \times (m+1)], \tag{4}$$

where n and m are chosen to vary the maximum power of variables, 'r' and 'z'. All approximating functions in the u direction must include an 'r' term because they describe an axisymmetric displacement. In the w direction the functions are formed slightly differently,

$$\phi_1^w = (z+1), \quad \phi_k^w(r, z) = \sum_{i=0}^{s} \sum_{j=0}^{t} \left[r^i(z+1)(z-1)z^j\right] + (z+1), \quad k = 2..[(s+1) \times (t+1)], \tag{5}$$

where again, s and t are chosen to vary the maximum power of variables 'r' and 'z' . All terms for the w direction need not include an 'r' term. However, any term multiplied by 'r' is forced to zero at $z = +1$ to satisfy the imposed boundary condition of uniform axial displacement of the top plate. Alternatively, the displacement in the w direction can only have a radial dependence from $-1 < z < +1$. Substitution of approximation functions in Eq. (3) into the weak form of the governing equations yields an eigenvalue problem of the form

$$([K] - \rho\omega^2[M])\{p\} = \{0\}. \tag{6}$$

The vector $\{p\}$ contains the coefficients b and d from Eq. (3) which correspond to different cylinder mode shapes. The explicit forms of matrices $[M]$ and $[K]$ in terms of ϕ^u and ϕ^w are reported by Heyliger in Ref. [7].

2.2. Numerical results for a single cell

Numerical simulations were performed for a single cell to compare the natural frequency predictions using the Ritz method to axisymmetric finite element results. The first and second modes were examined, because these modes are the component mode shapes important to the nth and $(n+1)$th isolator modes, respectively. An n-celled isolator is illustrated in Fig. 1. The boundary conditions were fixed-free, as illustrated in Fig. 2. The general material properties used were: $G_{metal} = 100\,\text{Pa}$, $v_{metal} = 0.3$, $\rho_{metal} = 10\,\text{kg/m}^2$, $G_{elas} = 1\,\text{Pa}$, $v_{elas} = 0.5$, $\rho_{elas} = 1\,\text{kg/m}^3$, $t_{elas} = 1\,\text{m}$, and $d_{cell} = 1\,\text{m}$. Note that the units for ρ_{metal} are mass per unit area, as appropriate for a vanishingly thin metal layer.

The axisymmetric finite element model consisted of parabolic quadrilateral axisymmetric elements, with 20 elements across the radius, and 20 elements through the thickness of the elastomer layer. The strain in the metal layer is insignificant, and thus only 5 elements are used across its thickness. This number of elements was found to be sufficient for convergence over the frequency range of interest. The frequencies calculated using the finite element analysis were $f_{n1} = 0.094\,\text{Hz}$ and $f_{n2} = 0.917\,\text{Hz}$. These values are used in subsequent comparisons to the Ritz predictions as baseline cases.

Table 1
Single cell natural frequencies using Ritz method compared to converged axisymmetric FEM results

$r^q \to q$	$z^p \to p$	2		3		4		5	
		(Hz)	% Error	(Hz)	% Error	(Hz)	% Error	(Hz)	% Error
1	f_{n1}	0.4594	388	0.0983	4.5	0.0982	4.4	0.0959	2.0
	f_{n2}	11.254	1128	5.6200	513	0.9745	6.3	0.9744	6.3
2	f_{n1}	0.4594	388	0.0982	4.5	0.0981	4.4	0.0951	1.2
	f_{n2}	11.254	1128	5.4220	491	0.9379	2.3	0.9377	2.3
3	f_{n1}	0.4594	388	0.0982	4.5	0.0981	4.3	0.0950	1.1
	f_{n2}	11.247	1127	5.4211	491	0.9338	1.9	0.9335	1.8

Table 2
Rate of Convergence Comparison for a Single Cell

Ritz method			Axisymmetric FEM		
Total d.o.f.	f_{n1} (Hz)	f_{n2} (Hz)	Total d.o.f.	f_{n1} (Hz)	f_{n2} (Hz)
3	0.4594	11.254	10	0.4576	6.761
10	0.0983	5.6200	32	0.1041	4.068
21	0.0981	0.9379	66	0.1002	1.005
36	0.0950	0.9335	170	0.0967	0.9536
55	0.0943	0.9179	640	0.0948	0.9269
78	0.0942	0.9177	2480	0.0940	0.9168

The first and second natural frequencies calculated with the Ritz method are presented in Table 1. A percent error is also calculated with reference to the axisymmetric finite element predictions. Combinations of the powers of the 'r' and 'z' polynomials are used in the approximating functions for both U_r and U_z. To simplify the tabular results, the power of 'r' in both the U_r and U_z approximating functions is the same for a given result. Similarly, the power of 'z' is the same in both the radial and vertical approximating functions. As can be observed from Eq. (4), the lowest possible power of 'z' in the radial direction is 2. This is therefore the lowest power used for both directions.

As seen in Table 1, as the powers of 'r' and 'z' increase, the Ritz predictions appear to converge to the axisymmetric finite element results. Table 2 lists the rates of convergence for both methods. The first and second natural frequencies of a single cell are computed for different number degrees of freedom in the elastomer layer. The Ritz method is observed to be significantly more accurate per degree of freedom.

For computational efficiency, the size of the eigenvalue problem should not be excessively large. Therefore, a frequency prediction with an error of 5% or less is deemed acceptably accurate for the current analysis. The lowest power case where this occurs for both modes 1 and 2, is a power of 2 for 'r', and a power of 4 for 'z'.

To further reduce the size of $[M]$ and $[K]$ in Eq. (6), higher-order approximating functions can be removed from both U_r and U_z. The powers of 'r' and 'z' in Table 3 were found to be sufficient to maintain at most a 5% error for the first and second natural frequencies.

Table 3
Reduced powers of 'r' and 'z' for U_r and U_z to approximate beginning and end stop band frequencies to within 5% error

	Power	
U_r	$r = 2$, $z = 3$	$n = 2$, $m = 1$ in Eq. (4)
U_z	$r = 1$, $z = 4$	$s = 1$, $t = 2$ in Eq. (5)

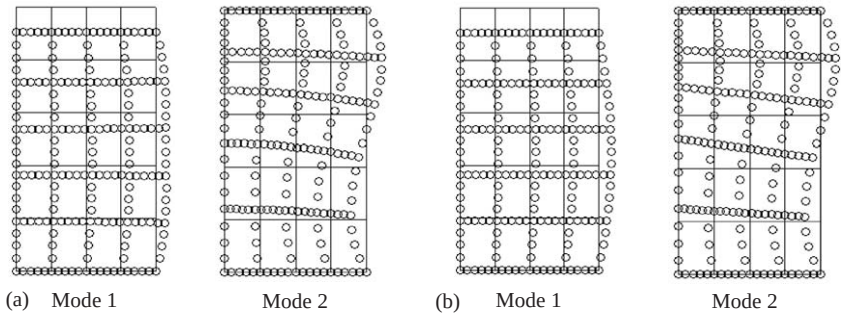

Fig. 3. Approximations for modes 1 and 2 of a single cell for, (a) higher order, U_r: power of 'r' = *3*, 'z' = 5, U_z: power of 'r' = 3, 'z' = 5, and (b) lower order, U_r: power of 'r' = 2, 'z' = 3, U_z: power of 'r' = 1, 'z' = 4.

The approximate value of the first natural frequency was in error by 4.5%. Likewise, the prediction of the second frequency was in error by 2.33%. In Fig. 3, the lower order mode shapes appear to be reasonably good approximations of the higher order mode shapes.

2.3. Analysis of layered isolators using component mode method

A method is developed in Ref. [8] for analyzing complex structures that can be divided into interconnected components. For this work, a single component is considered to be a combination of an elastomer and metal layer, or a cell in a periodically layered isolator. All strain is considered to be in the elastomer portion of the cell. Displacements of each cell are expressed in terms of generalized co-ordinates, $\{p\}$, and are defined by assumed displacement modes, as in Ref. [7]. In this work, the assumed modes take the form of Eqs. (4) and (5) and include a rigid-body mode in the z direction equal to unity. This mode allows for rigid-body motion of cells when interconnected.

When continuity conditions are imposed at cell boundaries, a set of constraint equations results which expresses kinematic relationships among the co-ordinates associated with different cells [8]. These constraint equations are used to determine a set of overall system (isolator) generalized co-ordinates equal to the total number of cell co-ordinates minus the number of constraint equations. The relationship between the sets of cell generalized co-ordinates and the set of isolator generalized co-ordinates is expressed in the transformation matrix, $[\beta]$. Isolator mass, stiffness, and damping matrices are obtained through this transformation. Forces on component cells are

also transformed into total system forces in this way. A set of equations of motion for the entire isolator results.

The procedure used to obtain isolator equations of motion, as presented by Hurty [8], is summarized here. The equation of motion for the sth cell of the isolator can be expressed as

$$[m]_s\{\ddot{p}\}_s + [c]_s\{\dot{p}\}_s + [k]_s\{p\}_s = \{P(t)\}_s, \tag{7}$$

where $\{p\}_s, \{\dot{p}\}_s, \{\ddot{p}\}_s$ are the column vectors of cell generalized displacements, velocities, and accelerations; $[m]_s, [c]_s, [k]_s$ are the square matrices of cell generalized masses, damping, and stiffnesses; and $\{P(t)\}_s$ is the column vector of generalized forces applied to the sth cell. These include forces transmitted through constraints as well as externally applied forces [8].

Using Eq. (7), equations are written for all isolator cells. The sets of cell equations of motion are grouped together in matrix form to create a total isolator set of equations:

$$[m]\{\ddot{p}\} + [c]\{\dot{p}\} + [k]\{p\} = \{P(t)\}. \tag{8}$$

When forming $[m]$, $[c]$, and $[k]$, it is desirable to group cell generalized co-ordinates together, as in

$$\{p\} = \begin{Bmatrix} \{p\}_1 \\ \{p\}_2 \\ \cdot \\ \cdot \\ \{p\}_r \\ \{p\}_s \\ \cdot \\ \cdot \end{Bmatrix}, \quad \{P(t)\} = \begin{Bmatrix} \{P(t)\}_1 \\ \{P(t)\}_2 \\ \cdot \\ \cdot \\ \{P(t)\}_r \\ \{P(t)\}_s \\ \cdot \\ \cdot \end{Bmatrix}. \tag{9}$$

Grouped in this way, the mass matrix takes the form

$$[m] = \begin{bmatrix} [m]_1 & \cdot & \cdot & \cdot & \cdot & \cdot & \cdot & 0 \\ \cdot & [m]_2 & & & & & & \cdot \\ \cdot & & \cdot & & & & & \\ \cdot & & & \cdot & & & & \cdot \\ \cdot & & & & [m]_r & & & \cdot \\ \cdot & & & & & [m]_s & & \cdot \\ \cdot & & & & & & \cdot & \cdot \\ 0 & \cdot & \cdot & \cdot & \cdot & \cdot & \cdot & \cdot \end{bmatrix}. \tag{10}$$

The damping and stiffness matrices take a similar form [8]. Eq. (8) can be considered a group of unconnected sets of cell equations of motion. When displacement constraints are imposed at cell boundaries, a set of constraint equations results among the elements of $\{p\}$. If there are m elements in vector $\{p\}$, and k constraint equations relating them, then there will be $n = m - k$ independent co-ordinates in the isolator equations of motion. This independent set of isolator co-ordinates is designated $\{q\}$, and is directly related to $\{p\}$ through a linear transformation. The

transformation can be derived such that

$$\{p\} = [\beta]\{q\}. \tag{11}$$

The transformation matrix, $[\beta]$, has dimensions $m \times n$ where $m > n$. The construction of matrix $[\beta]$ can be completed with knowledge of the displacement constraints among the isolator cells. Suppose that a displacement constraint exists between cell r and s, such that

$$\bar{u}^r(r, z = -1) = \bar{u}^s(r, z = 1) \tag{12}$$

If all displacement constraints between cells are written in terms of vector $\{p\}$, then the entire set of constraints can be written in matrix form as

$$[A]\{p\} = \{0\}, \tag{13}$$

where $[A]$ is a rectangular matrix with dimensions $k \times m$. Because $m > k$, $[A]$ may be partitioned as

$$[A] = [A_1|A_2], \tag{14}$$

where $[A_1]$ is a square matrix with dimensions $k \times k$, Eq. (13) can then be rewritten as

$$[A_1]\{p\}_d + [A_2]\{p\}_f = \{0\}. \tag{15}$$

Here, $\{p\}_d$ and $\{p\}_f$ are subsets of $\{p\}$ and are the dependent and independent variables, respectively. The subsets must be chosen such that matrix $[A_1]$ is non-singular, or invertible [8]. The dependent variables can then be explicitly expressed in terms of the independent variables as

$$\{p\}_d = -[A_1]^{-1}[A_2]\{p\}_f. \tag{16}$$

From this, the relationship between the entire set isolator variables, $\{p\}$ and the independent set, $\{p\}_f$ can be derived as

$$\{p\} = \begin{Bmatrix} p_f \\ p_d \end{Bmatrix} = \begin{bmatrix} [I] \\ \hline -[A_1]^{-1}[A_2] \end{bmatrix} \{p\}_f. \tag{17}$$

Eq. (17) can be rewritten, and thus the transformation can be stated as

$$\{p\} = [\beta]\{p\}_f. \tag{18}$$

Substituting Eq. (18) into Eq. (8) and premultiplying all terms by $[\beta]^{\mathrm{T}}$, the isolator equations of motion can be stated:

$$[\beta]^{\mathrm{T}}[m][\beta]\{\ddot{p}\}_f + [\beta]^{\mathrm{T}}[c][\beta]\{\dot{p}\}_f + [\beta]^{\mathrm{T}}[k][\beta]\{p\}_f = [\beta]^{\mathrm{T}}\{P(t)\}. \tag{19}$$

To perform this substitution, the vector $\{p\}$ has been arranged so that all dependent variables are below the independent variables. Therefore, the rows and columns of original matrices $[m]$, $[c]$, $[k]$ and rows of vector $\{P(t)\}$ must be rearranged accordingly. The following identities can be defined [8]:

$$[M] = [\beta]^{\mathrm{T}}[m][\beta], \tag{20}$$

$$[C] = [\beta]^{\mathrm{T}}[c][\beta], \tag{21}$$

$$[K] = [\beta]^{\mathrm{T}}[k][\beta], \tag{22}$$

$$\{Q(t)\} = [\beta]^{\mathrm{T}}\{P(t)\}. \tag{23}$$

An eigenvalue analysis can then be performed using the system matrices $[M]$ and $[K]$ to obtain the n^{th} and $(n+1)$th natural frequencies. These correspond to the beginning and end stop band frequencies.

3. Experiment

Experimental tests were performed for various layered test specimens to verify the analytical prediction method. The experiments were performed by attaching a given specimen to a rigid base, which in turn was attached to a mechanical shaker. The shaker input was a series of chirp signals each spanning 400 Hz. To measure the transmissibility of a test specimen, one accelerometer was placed on top of the specimen, and another was placed on the rigid base. The signals were then fed into a Fourier analyzer. In this way, the specimen transmissibilities were directly measured. The experimental set-up is pictured in Fig. 4.

The first specimen initially consisted of 4 cells. The elastomer was a lightly damped material and the metal layer was steel. The elastomer material properties were $G_e = 0.6\,\text{MPa}$, and $\rho_e = 1000\,\text{kg/m}^3$. The elastomer was assumed to be incompressible, which corresponds to a Poisson ratio of $\nu = 0.5$. To avoid mathematical singularities, the Poisson ratio was approximated at $\nu = 0.499$. The specimen geometry was $t_e = 1\,\text{cm}$, $t_m = 1\,\text{cm}$, and $d = 4\,\text{cm}$. This geometry corresponds to an elastomer shape factor of 1. The important specimen properties are summarized in Table 4.

In Fig. 5, the experimental and analytical transmissibilities are plotted for specimen 1 with four layers. The elastomer had not been characterized at high frequencies, and thus an initial estimate of the shear modulus for analytical predictions was obtained from initial low-frequency

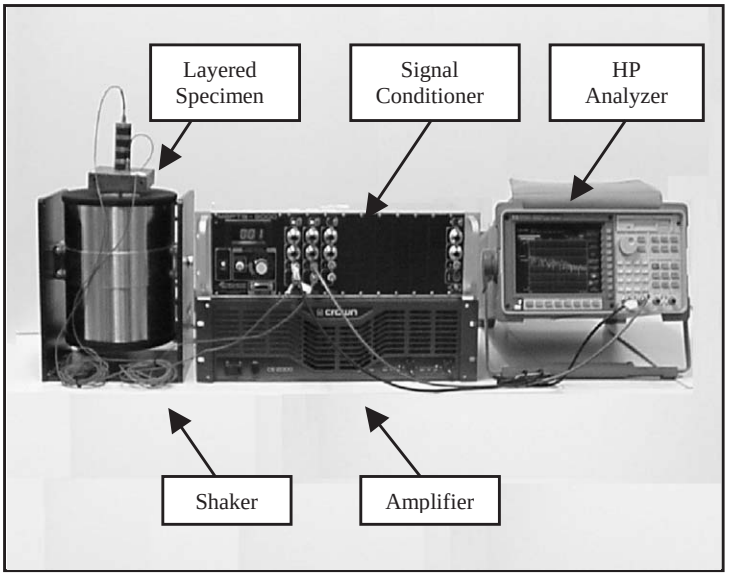

Fig. 4. Experimental set-up.

Table 4
Summary of specimen properties

	Specimen 1	Specimen 2	Specimen 3
d (cm)	4.0	2.54	4.0
t_{elas} (cm)	1.0	1.0	1.0
t_{steel} (cm)	1.0	0.64	1.0
G_{elas} (MPa)	0.6	0.6	3.06
Loss Factor (η)	0.05	0.05	0.15

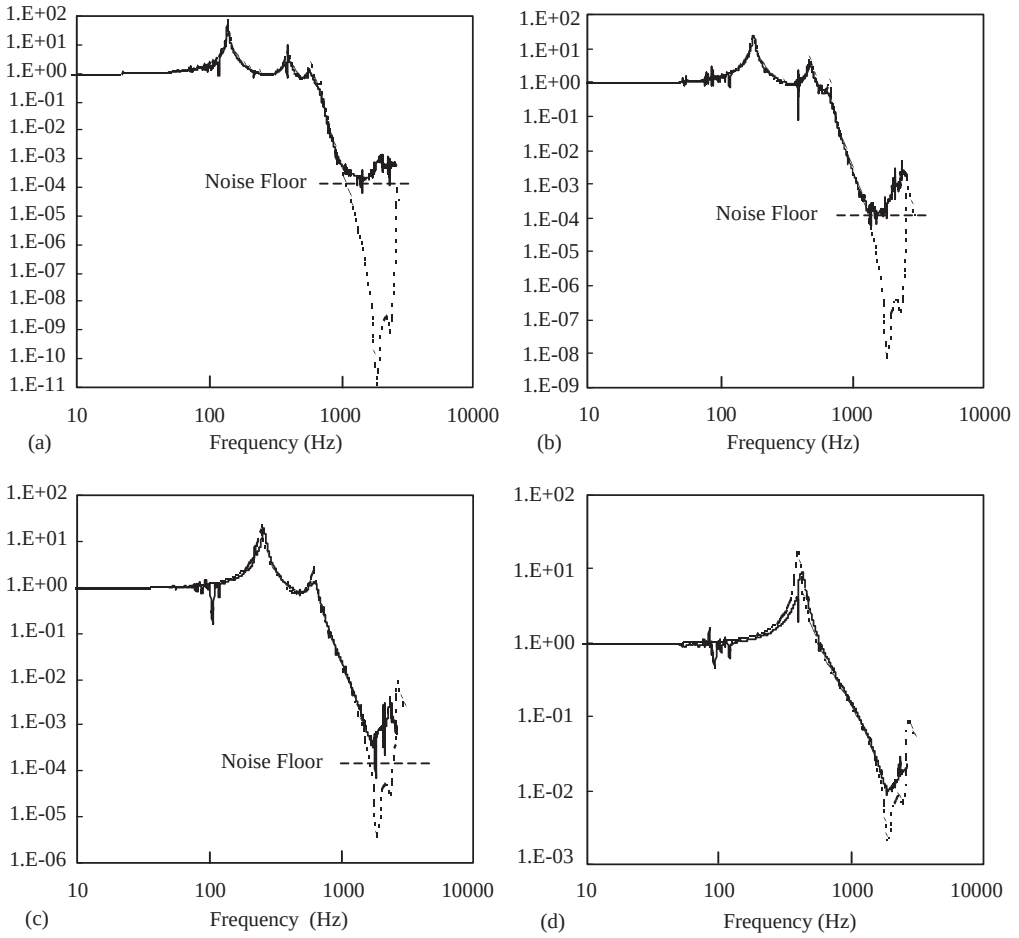

Fig. 5. Experimental and analytical transmissibilities for specimen 1 for (a) 4 cells, (b) 3 cells, (c) 2 cells, and (d) 1 cell: —, experimental, - - -, analytical.

characterization. The shear modulus was then adjusted so that the analytical plot matched the experimental results near the beginning of the stop band. Similarly, the loss factor was estimated at 0.05 by matching resonant peak height. To validate the analytical method, the resulting

material property values were to be used to predict transmissibilities of an additional specimen composed of the same elastomer, but having a different geometry. Although the model accommodates frequency-dependent material properties, using constant values for the test frequency range was adequate to validate the analytical method.

In Fig. 5(a)–(d), experimental and analytical results are shown for specimen 1 with 4, 3, 2, and 1 cells. For all cases, the first n resonant peaks are nearly coincident. The stop band locations are also accurately predicted. For the 4, 3, and 2 cell cases, a discrepancy exists between experiment and the analytical predictions for stop band depth. This discrepancy may be because of the existence of an experimental noise floor, below which transmissibilities cannot be accurately measured.

The second specimen tested consisted of 4 cells, as well. The elastomer used was the same as in specimen 1. The metal layer was again steel. The specimen geometry was changed to $t_e = 1\,\text{cm}$, $t_m = 0.64\,\text{cm}$, and $d = 2.54\,\text{cm}$. This geometry corresponds to an elastomer shape factor of 0.64.

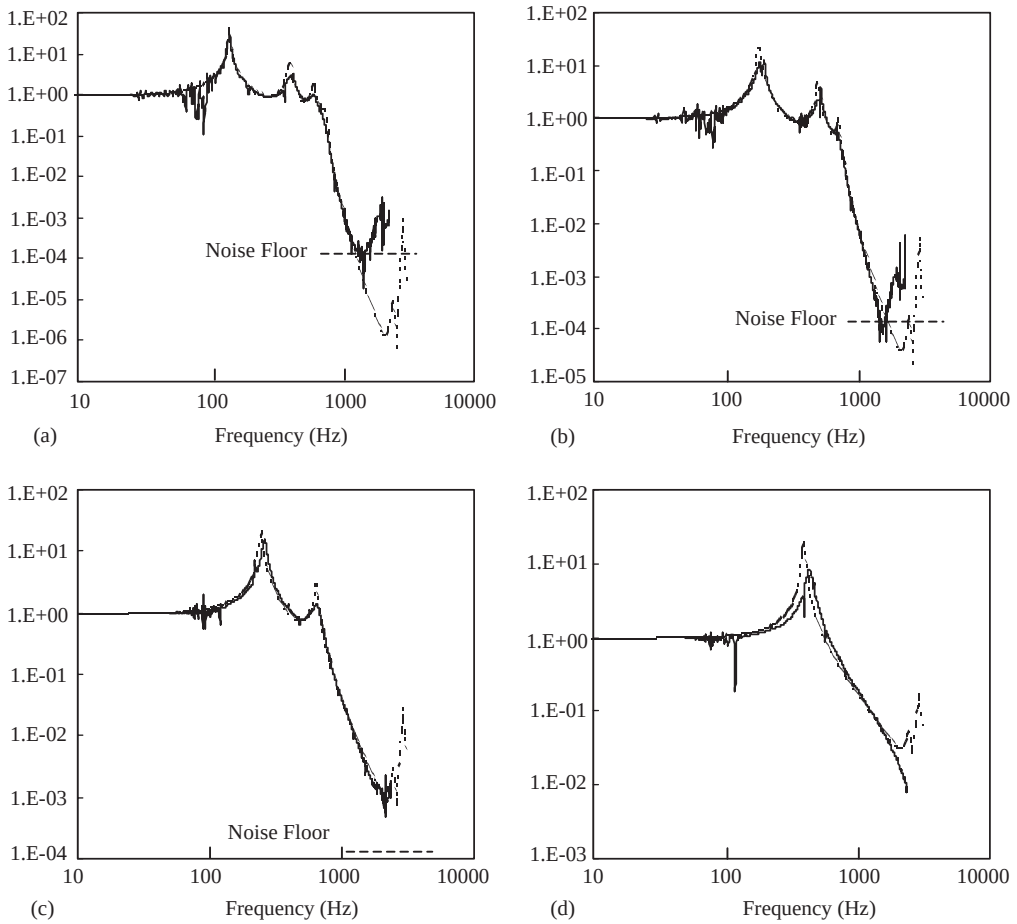

Fig. 6. Experimental and analytical transmissibilities for specimen 2 for (a) 4 cells, (b) 3 cells, (c) 2 cells and (d) 1 cell: —, experimental, - - -, analytical.

By changing the geometry of the second specimen, but using the same elastomer as in specimen 1, the analytical method was to be validated.

In Fig. 6, experimental and analytical transmissibilities are plotted for specimen 2, with varying numbers of cells. For the analytical predictions, the same value of shear modulus was used as determined for specimen 1. Similar to specimen 1, the results for specimen 2 show a discrepancy between experimental and analytical results for stop band depth in the 4 cell case. However, the predictions for the 3, 2, and 1 cell cases are nearly colinear with experimental results over the entire frequency range.

In Figs. 5 and 6, a transmissibility noise floor of 1.4×10^{-4} is shown. The noise floor is calculated using the relation

$$NF = \frac{(a_{\min})_{top}}{(a_{\max})_{bot}} = \frac{a_{res}}{(a_{\max})_{bot}}, \tag{24}$$

where a_{min} and a_{max} are the accelerations of the specimen top and bottom, respectively, and a_{res} is the accelerometer resolution, quoted at 0.005 g. The maximum experimental acceleration of the specimen base was measured to be 36 g at 1.5 kHz. The minimum measured transmissibility for the 3 and 4 cell cases may have been obscured by the presence of a noise floor.

The results in Figs. 5 and 6 show that the analytical model can accurately predict the locations of the beginning stop band frequencies, assuming that the correct material properties are known. The experimental end frequencies are not well defined and, as a result, the accuracy of the end frequency prediction is difficult to assess. The model accurately predicts stop band depths for both 1 cell cases, as well as the 3 and 2 cell cases for specimen 2. The minimum measured stop band depth for both the 3 and 4 celled cases is a transmissibility of around 1×10^{-4}, or nearly coincident with the noise floor. Although the minimum measured transmissibility may have been affected by the noise floor, this attenuation factor of 10,000 would be sufficient for most vibration control applications.

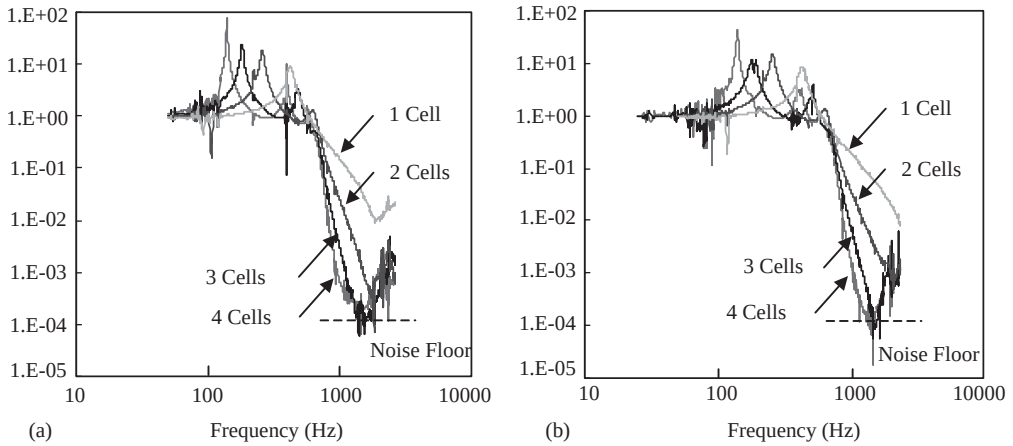

Fig. 7. Comparison of experimental transmissibilities for varying number of cells for (a) specimen 1, (b) specimen 2.

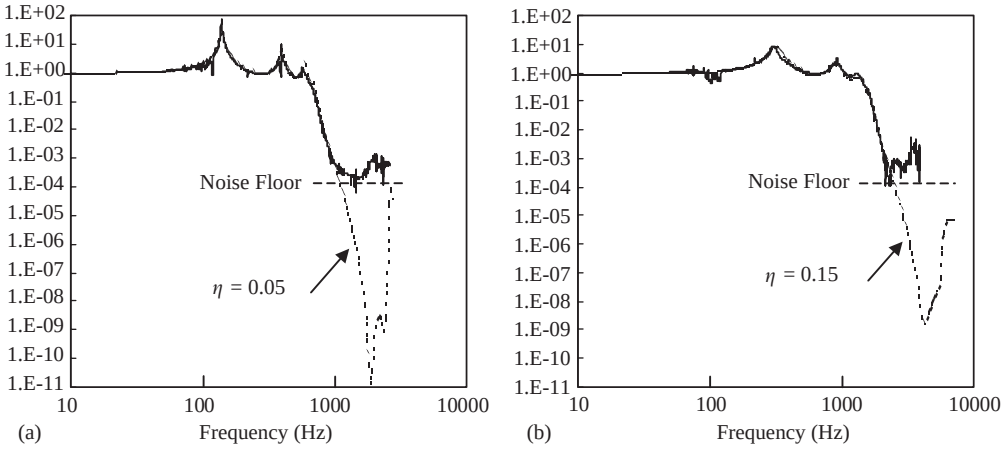

Fig. 8. Experimental and analytical 4-celled transmissibilities of (a) specimen 1, (b) specimen 3: —, experimental, - - -, analytical.

In Fig. 7, experimental transmissibilities are compared for varying number of layers for both specimens 1 and 2. Comparing the stop band depths of both the 1 and 2 cell cases, a full order of magnitude of reduction is gained with an increase of 1 to 2 cells for both specimens. Similarly, increasing from 2 to 3 cells reduces the transmissibility by an additional order of magnitude for both specimens. The effect of increasing the number of cells from 3 to 4, however, is not certain because of the noise floor location. Although the change in stop band depth cannot be reliably measured when going from 3 to 4 cells, the transmissibility roll-off rate following the beginning of the stop band is significantly increased. Therefore, a practical design could limit the minimum number of cells to three or four to ensure a pronounced stop band attenuation effect.

The effect of increased elastomer damping was also investigated. An additional layered specimen 3 was constructed that had the same geometry as specimen 1. An elastomer with approximately the same shear modulus as that used in specimen 1, but with a significantly higher loss factor, was desired. An elastomer having a modulus nearly identical to to that elastomer 1 at low frequencies was thus selected. Upon tuning the modulus to align the experimental and analytical results, however, it was found to be 400% higher than the low-frequency value. Nevertheless, a transmissibility comparison between specimens 1 and 3 is made in Fig. 8. The loss factor of elastomer 3 was approximately 0.15. The difference between the higher and lower damping is most noticeable when comparing the first resonant peaks of specimens 1 and 3. The first peak of specimen 1 is about a factor of 10 higher than that of specimen 3. Both specimen transmissibilities, however, reach an approximately equal minimum value between 1×10^{-3} and 1×10^{-4}. Although the minimum measured transmissibilities may coincide with the noise floor, only measurements within a relatively small frequency range would have been obscured within the stop bands. Also, the transmissibility roll-off does not change appreciably with higher damping. Therefore, the basic stop band attenuation characteristics do not appear to be significantly affected by the addition of modest damping.

4. Conclusions

A Ritz approximation method was developed to model the axisymmetric dynamic behavior of layered isolators. A single cell was modelled in a fixed-free condition, the first two modes of which are subsequently used to provide estimates for the beginning and end stop band frequencies. To accurately predict the first two natural frequencies of a cell to within 5% error, a certain minimum power of the variables, 'r' and 'z', was required for the both the radial and axial directions. For the radial direction, the powers of 'r' and 'z' were two and three, respectively. For the axial direction, they were one and four, respectively.

An n-celled isolator model was developed using the Ritz approximation method combined with a modal synthesis method. The natural frequencies were found to agree with 2-D axisymmetric finite element predictions. The model enabled the prediction the nth and $(n+1)$th isolator modes, which correspond to the stop band beginning and end frequencies.

The isolator model was validated with experiments. Experimental and analytical transmissibilities were compared for two specimens with the same elastomer, but different shape factors. The elastomer properties used for analytical predictions were determined by matching analytical and experimental transmissibilities of the first specimen. The properties were then used to predict the behavior of the second specimen. In both cases, the transmissibilities before the start of the stop band show close agreement. For the four and three cell cases, analytical transmissibilities lie below the experimental results, although the experimental noise floor may affect these results. A minimum experimental transmissibility of about 1×10^{-4} was observed for these three and four cell cases.

Experimental and analytical transmissibilities were also compared for two specimens fabricated with two different low modulus elastomers, one highly damped, and one lowly damped. The experimental results show that stop band effectiveness is not appreciably affected by addition of modest damping.

Acknowledgements

This research was supported by United Technologies Research Center, Technical Monitors — William Weller and Dr. Goldino Alves.

References

[1] J.C. Snowden. Vibration isolation: use and characterization. Applied Research Laboratory, The Pennsylvania State University, National Bureau of Standards Handbook 128, Washington, D.C., 1979, pp. 25–37.

[2] J.L. Sackman, J.M. Kelly, A.E. Javid, A layered notch filter for high-frequency dynamic isolation, Journal of Pressure Vessel Technology 111 (1989) 17–24.

[3] J.L. Sackman, J.M. Kelly, A.E. Javid, A layered notch filter for high frequency dynamic isolation, ASME, Pressure Vessels and Piping and Computer Engineerings Divisions, Conference and Exhibition, Chicago, IL, Vol. 113, 1986, pp. 55–64.

[4] A.K. Ghosh, Periodically layered composites for attenuation of dynamic loads, Nuclear Engineering and Design 84 (1985) 53–58.

[5] J.T. Szefi, E.C. Smith, G.A. Lesieutre, Analysis and design of high frequency periodically layered isolators in compression, 41st Structures, Structural Dynamics and Materials Conference, Atlanta, GA, 2000.
[6] J.T. Szefi, E.C. Smith, G.A. Lesieutre, Formulation and validation of a Ritz-based analytical model for design of periodically layered isolators in compression, Proceedings of the 42nd Structures, Structural Dynamics and Materials Conference, Seattlea, WA, 2001.
[7] P.R. Heyliger, Axisymmetric free vibrations of finite anisotropic cylinders, Journal of Sound and Vibration 184 (1991) 507–520.
[8] W.C. Hurty, Dynamic analysis of structural systems using component modes, American Institute of Aeronautics and Astronautics Journal 3 (1965) 678–685.